JOURNAL OF MATERIALS SCIENCE 22 (1987) 896–906

Combined X-ray microdiffraction and topography experiment for microstructural analysis of heterogeneous materials

M. RAPPAZ, E. BLANK
Laboratoire de métallurgie physique, Ecole Polytechnique Fédérale de Lausanne, Ch. de Bellerive 34, CH-1007 Lausanne, Switzerland

A new experimental set-up combining X-ray topography and microbeam diffraction has been designed for the investigation of heterogeneous microstructures with features in the size range of more than 50 μm. Built around a four-circle goniometer of 5/1000° angular resolution, this apparatus offers similar facilities to those obtained by TEM but at a different scale. In the Berg–Barrett position, grain and subgrain boundaries can be observed over large surface areas (typically 100 mm^2). Based on topography observations, areas of interest of typically 100 μm diameter can be precisely selected for microdiffraction measurements. A laser beam directed through the pinhole system of the X-ray microbeam collimating system permits one to directly visualize the irradiated zone. The divergence of the X-ray microbeam is typically 0.034° (full width at half maximum) and permits the measurement of lattice spacing variations ($\Delta a/a$) of the order of 10^{-4}. While TEM permits one to examine very localized areas, this new device is appropriate to detect long-distance effects and phase interactions in materials with coarse distributed heterogeneities. In order to demonstrate the versatility of this new device, the orientation distribution, variation of lattice spacing and mosaïc structure of dendrites in directionally solidified nickel-base alloys are analysed.

1. Introduction

Many problems in materials science are concerned with structural heterogeneities such as second-phase particles, grain boundaries or zones of localized plastic deformation. X-ray diffraction techniques used to study structural heterogeneities have been largely replaced over the last two decades by electron microscopy and electron diffraction, owing to the high power of spatial resolution of these latter techniques. Nevertheless, X-ray diffraction exhibits unique features which are outside the scope of TEM [1–3]. First, many of the disadvantages related to the preparation of thin films are avoided. In back-scattering, only one specimen surface needs to be prepared, and in transmission the specimen can be much thicker than in TEM, as a result of the comparatively large penetration depth of X-rays. X-rays thus provide a better tool for the investigation of bulk properties and problems involving internal stresses. Second, X-ray diffraction is more sensitive to lattice constant variations and lattice misorientations since the Bragg angles are large. And finally, X-ray diffraction techniques are particularly well suited for the analysis of structural features in the size range of about 10 μm up to macroscopic dimensions. This size range is outside the scope of TEM because the transparent area of thin films is very limited in size, particularly in the case of polyphase materials.

This paper deals with a new technique for the X-ray diffraction analysis of features in the size range of optical microscopy. The apparatus, which combines X-ray topography and X-ray diffraction facilities, allows one to position accurately an X-ray microbeam on selected features of microscopical dimensions. While making use of the advantages of X-ray analysis listed above, this device furnishes information similar to that obtained by TEM but at a different size scale. Berg–Barrett topographs [4], the equivalent of TEM dark-field observations, are recorded in a first step of investigation and compared with optical micrographs. Any zone of interest is then placed in line with an X-ray microbeam of typically 100 μm diameter. For this purpose the zone to be investigated is directly viewed with a laser beam directed through the same pinhole system as the X-ray beam. Lattice orientation, lattice spacing and line profiles of precisely located microstructural zones can be measured with high accuracy. Specimen surfaces of arbitrary size can be mapped by point-by-point measurements, thus allowing one to establish correlations between far distant microstructural features.

After a brief description of the experimental set-up (Section 2) and of its resolution (Section 3), a few applications are presented (Section 4). It will be shown in particular how this X-ray diffraction technique can be used to study microstructural inhomogeneities in as-solidified materials.

2. Apparatus

The apparatus has been designed to measure

0022–2461/87 $03.00 + .12

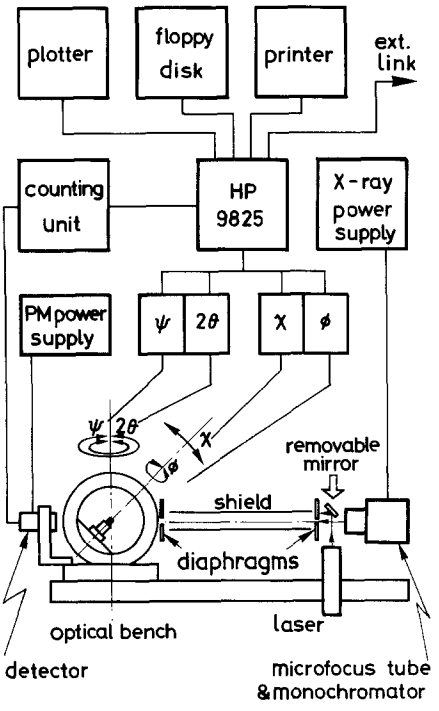

Figure 1 Schematic diagram of the experimental set-up for X-ray topography and X-ray microdiffraction.

the diffraction characteristics of single-crystalline domains of typically 100 μm diameter. The investigated zone can be part of a large single crystal containing microstructural inhomogeneities, or it can be a single grain within a coarse-grained polycrystalline material.

A schematic diagram of the apparatus is shown in Fig. 1. A Huber four-circle goniometer driven by stepping motors provides orientation of the specimen and positioning of the scintillation detector. The smallest step increment is 0.005^0 (18 seconds of arc) for each angle. The four motors and the counting unit are controlled by an HP 9825 microcomputer.

The X-ray microbeam is produced by a small-focus tube (0.8 mm × 0.15 mm when viewed at 60°) followed by a collimating system: the source diaphragm is directly attached to the X-ray tube and the specimen diaphragm in front of the specimen surface is mounted on the four-circle goniometer. In order to vary independently the beam divergence and the size of the irradiated zone, the distance between source and specimen can be changed from 0.3 to 1 m by translating the X-ray tube. Specimen diaphragms of different sizes (0.1 to 1 mm) are interchangeable without further adjustment. In order to reduce vibrations and maintain alignment, the whole experiment is mounted on an optical bench made of granite.

The four-circle goniometer is considered as the reference frame and must be by itself very well adjusted. The $2\theta = 0°$ line of the X-ray beam is given by the specimen diaphragm and the detector diaphragm when this latter is positioned at $2\theta = 0°$. X-ray source and collimator are adjusted to the $2\theta = 0°$ line using x–y micrometric translation stages operating in a plane perpendicular to the beam. Furthermore, the X-ray tube may be rotated along a vertical axis for adjustment of the source viewing angle.

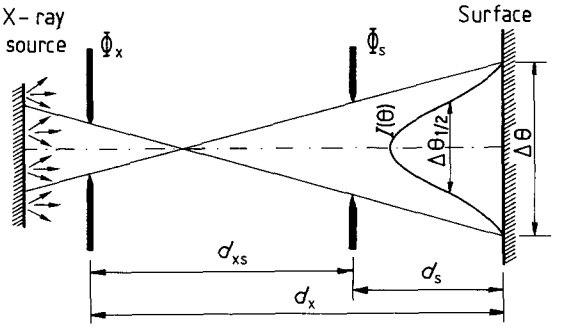

Figure 2 Divergence of the X-ray beam.

In microdiffraction experiments, the source is placed at about 40 cm from the goniometer centre. If Φ_x and Φ_s are the diameters of the X-ray source diaphragm and of the specimen diaphragm, respectively, then the beam divergence is given [5] by

$$\Delta\theta_{\mathrm{FWHM}} = \frac{\Phi_x \Phi_s}{\Phi_x d_s + \Phi_s d_x} \qquad (1)$$

d_x and d_s measure the distances of the two diaphragms with respect to the specimen surface (see Fig. 2). The divergence calculated in this way corresponds to the full width at half maximum (FWHM) of the intensity. The overall divergence of the beam $\Delta\theta$ is simply given by

$$\Delta\theta = \frac{\Phi_s + \Phi_x}{d_{xs}} \qquad (2)$$

where d_{xs} is the distance between the two diaphragms.

When recording topographs, the circular specimen diaphragm is replaced by cross-slits and the source is removed from the specimen surface (typically 1 m). In such cases, a vacuum tube with thin mica windows at both ends is inserted between the source and the specimen diaphragms. The tube reduces absorption of the X-ray beam in air by a factor of about 2. Furthermore, it provides an efficient protection against accidental handling in the X-ray beam.

As discussed in more detail in the next section, use of a monochromator was unnecessary for most of the specimens investigated so far. Thus, generally, Cu$K\alpha$ filtered radiation was used. If needed, a silicon monochromator with asymmetrical (1 1 1) diffraction was inserted to separate the $K\alpha_1$–$K\alpha_2$ doublet. The monochromator surface being cut at 9° from the (1 1 1) plane, the viewed X-ray source was reduced to 0.15 mm × 0.15 mm for diffractometric studies or was enlarged to 4 mm × 0.15 mm when used the other way around for topographic observations. However, any use of the monochromator and of small diaphragms considerably reduces the beam intensity.

Selection of the irradiated zone for microdiffraction measurements is achieved with a laser beam directed through the same pinhole system as the X-ray beam, see Fig. 3. In order to direct the laser with adjustable mirrors was designed. A 2 mW He–Ne laser is mounted vertically, i.e. perpendicular to the X-ray beam (see Fig. 3). In order to direct the laser beam precisely through the source- and specimen diaphragms, two translational and two rotational fine

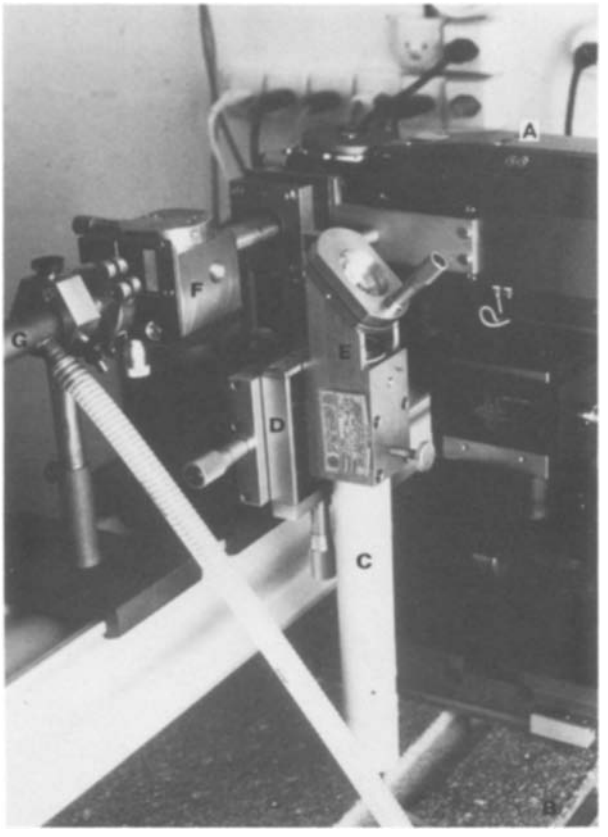

Figure 3 View of the laser and of the optical/X-ray by-pass. A: X-ray tube, B: granite bench, C: He–Ne laser, D: x–y translation stage of the laser, E: laser housing and first mirror, F: optical/X-ray by-pass, G: vacuum tube (only used for X-ray topography).

adjustments are required. For that purpose, the laser is set on an x–y micrometric stage. A mirror directly attached to the laser housing deviates the beam by 45° and thus provides one of the two rotational operations. A second adjustable mirror is mounted in the bypass (Fig. 4). When set precisely in a 45° position as shown in Fig. 4, it orients the laser beam in the proper direction, i.e. through the pinhole system. It is placed within a cylindrical cavity and attached to a rotating cover, thus preventing any X-ray radiation from coming out. When the cover is rotated by 45° (0° position), the X-ray beam goes through the bypass since the mirror is off-centred by 3 mm with respect to the cover rotation axis.

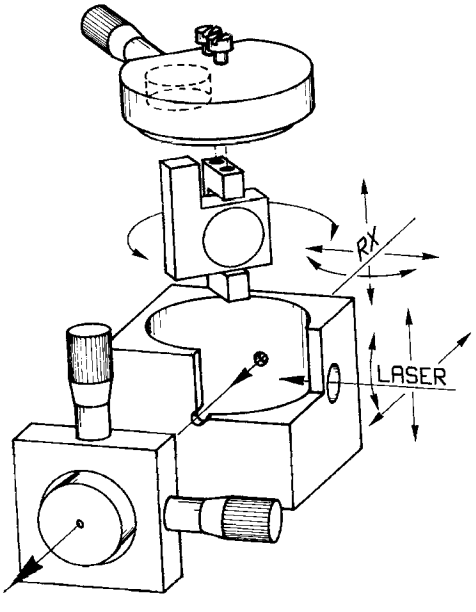

Figure 4 Three-dimensional view of the X-ray/laser by-pass. The mirror is used to select X-rays (at 0°) or laser beam (at 45°) as well as one of the four adjustments required to precisely align the laser beam on the $2\theta = 0°$ line.

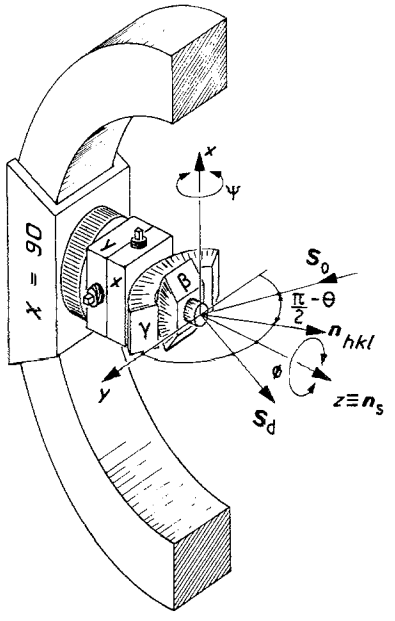

Figure 5 Three-dimensional view of the specimen mounting ($\chi = 90°$ position). The angles β and γ are used to align the specimen surface normal $\boldsymbol{n}_s$ on the ϕ-rotation axis. The angles ϕ and ψ are then used to orient the specimen in the desired diffraction position. $\boldsymbol{s}_0$: incident beam, $\boldsymbol{s}_d$: diffracted beam. The x and y translation axes of the goniometer head are used to select the irradiated zone of the specimen surface.

A microscope attached to the four-circle goniometer permits one to see the spot of the laser on the specimen surface. This spot has about the size of the specimen diaphragm if this latter is placed close to the surface so that associated optical diffraction is minimized. The laser proved to be also very helpful to align the experiment, in particular the pinhole system, and to adjust the specimen surface at the centre of the goniometer.

A three-dimensional view of the specimen mounting is shown in Fig. 5. The specimen, exhibiting an electropolished flat surface, is attached to a standard goniometer head. In microdiffraction, mounting of the specimen requires fulfilment of the following two conditions: first, the irradiated zone must be at the centre of the four-circle goniometer in order to measure correct values of 2θ; second, the normal to the specimen surface $\boldsymbol{n}_s$ must be perpendicular to the x–y plane because scanning of the specimen surface (which is done by translation of the specimen along the x- and y-axes of the goniometer head) should not violate the first condition. This last setting is achieved by adjusting the angles β and γ of the goniometer head until a ϕ rotation no longer changes the position of the laser beam reflected by the specimen surface. The height z of the specimen is then varied until the location of the laser spot on the specimen surface remains unchanged while the specimen is rotated around the ϕ axis.

The $\chi = 90°$ position (i.e. $\boldsymbol{n}_s$ in the plane containing the incident beam $\boldsymbol{s}_0$ and the diffracted beam $\boldsymbol{s}_d$) was chosen for convenience: it corresponds to the zero-layer condition of Berg–Barrett topography [4].

Moreover, the (ψ, ϕ) angles used to bring into diffraction the desired ($h\,k\,l$) planes directly measure the spherical coordinates of the normal $\boldsymbol{n}_{hkl}$ in a reference frame where the z axis corresponds to the normal of the specimen surface.

In diffraction, the accuracy of specimen setting directly influences the precision of 2θ value measurements (see Appendix). Using the laser beam facility, the height and orientation of the specimen surface can be adjusted to typically $\pm 10\,\mu$m and $\pm 0.05°$, respectively. With a surface-to-detector distance of about 200 mm, positioning errors within these limits correspond to an error in $\Delta a/a$ of about one motor-step (0.005°). This error is minimized when working in asymmetric reflection, the larger angle being measured between the incident beam and the specimen surface (angle $(\theta + \alpha)$ in the Appendix, where α is the angle between the ($h\,k\,l$) diffraction planes and the surface). A large $(\theta + \alpha)$ angle corresponds also to an irradiated spot of small size. This "microdiffraction position" is opposite to the Berg–Barrett position used to record topographs. In this latter case, $(\theta - \alpha)$ is chosen as incident angle, i.e. 180° rotation about the normal $\boldsymbol{n}_{hkl}$ to the diffracting planes (see Fig. 11), in order to increase the width of the irradiated zone and to facilitate positioning of the film.

Usually, the following procedure is used in X-ray microstructural analysis:

(i) After metallographic preparation and electropolishing, the specimen is mounted on the goniometer head.

(ii) Using the laser, the height and the orientation of the surface are adjusted on the four-circle goniometer so that the two conditions mentioned before are fulfilled.

(iii) Removing the goniometer head, a Laue photograph is taken on a separate instrument. The digitized Laue spots are then analysed by the HP 9825 microcomputer driving the four-circle goniometer. The result of the analysis is a matrix of crystallographic direction cosines measured in a reference frame attached to the specimen (the z-direction coincides with the specimen surface normal $\boldsymbol{n}_s$).

(iv) After replacing the goniometer head on the four-circle goniometer, either topographs can be recorded on a film or intensity can be measured as a function of various angles. Using the matrix of direction cosines, the computer determines the angular settings of the four-circle goniometer for any ($h\,k\,l$) reflection and then rotates the sample and the detector according to these calculations.

(v) Any zone of interest is selected by using the laser, the translation stage of the goniometer head and the microscope attached to the four-circle goniometer.

(vi) In microdiffraction, the intensity can be measured in the entire reciprocal space, i.e. by varying simultaneously ϕ, ψ and 2θ. However, it is usually sufficient and much faster to record two line profiles around the maximum of intensity. Once this maximum has been found by a semi-automatic procedure, a program permits one to record rocking curves and/or θ–2θ line profiles. The results are stored on floppy disks for further treatment of data.

(vii) Going back to step (v), any other zone can be selected.

By making use of the combination of X-ray topography and microbeam diffraction, different modes of operation are possible, furnishing results at different levels of sophistication. In recording topographs, for example, sample and film may be rocked during exposure within a certain angular interval. This technique, which represents some kind of texture analysis, simultaneously provides information about the spatial and angular distributions of microstructural features.

3. Sensitivity

The angular resolution of this new experimental set-up and the precision of the specimen setting were tested for various crystals, in particular silicon, germanium and a nickel-base alloy.

Fig. 6 presents the (0 0 4) diffraction line profiles of a quasi-perfect (0 0 1)-oriented silicon single crystal, using Cu$K\alpha$ filtered radiation. The collimator diaphragms Φ_x and Φ_s, which were separated by a distance d_{xs} = 190 mm, had diameters of 0.1 and 0.15 mm, respectively. The cross-slits of the detector were 0.15 mm large in the diffraction plane (i.e. the plane containing the incident and the diffracted beams) and 2 mm in the perpendicular direction. The dashed line corresponds to a rocking curve (variation of the ψ angle only) while the solid curve is a standard θ–2θ profile. In both cases, the recorded intensity is plotted against the ψ (or θ) angle. The ψ angle steps clearly visible on Fig. 6 correspond to the smallest step-motor increment (0.005°).

The maximum value of the intensity which is associated with the $K\alpha_1$ component of copper radiation (λ = 0.154056 nm) [6] is situated at 2θ = 69.125°. This corresponds to a lattice parameter of a_0 = 0.54312 nm a value which is in good agreement with

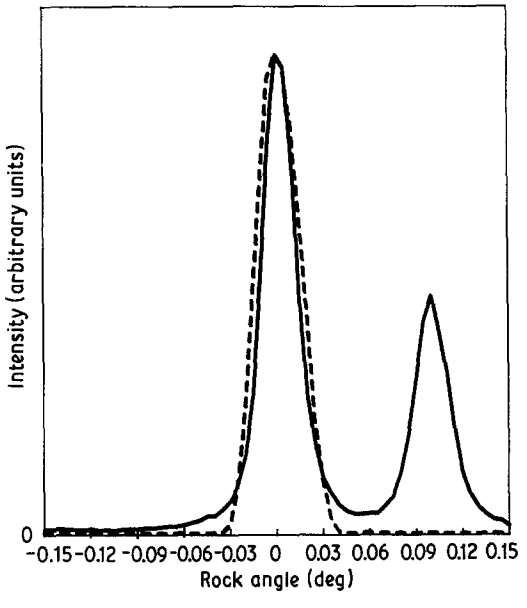

Figure 6 (– – –) Rocking curve and (——) θ–2θ line profile of the (0 0 4) reflection of a (0 0 1) silicon specimen. Cu$K\alpha$ radiation. ψ = 34.5625° ± 0.15°. Φ_x = 0.1 mm, Φ_s = 0.15 mm, detector cross-slit 0.15 mm × 2 mm, d_{xs} = 190 mm, d_s = 20 mm, D = 200 mm. Counting time: 2 sec. for each step.

the literature ($a_0 = 0.54309$ nm at 25° C [6]). According to Equation A3, with a specimen-to-detector distance $D = 200$ mm, a difference of $\Delta a/a = 5.5 \times 10^{-5}$ between measured and reference value would correspond to a misalignment of 9 μm in the specimen height. This value can be taken as an indication for the precision of the specimen setting required in microdiffraction experiments. It should be noted that this difference of $\Delta a/a$ is in fact smaller than the corresponding value obtained by one step-motor increment (0.005°). Beam misalignment is certainly of the same order of magnitude. On the other hand, a symmetric diffraction with a small θ value (34.5625°) is not the best suited for precise measurements of lattice spacings.

Using the (0 0 4) setting, it was possible to translate the silicon single crystal by ± 3 mm in the x and y directions without shifting the 2θ position of the diffraction peak by more than 0.02° (four steps of the motors). Using the formula given in the Appendix (Equation A4), this means that misalignment between the specimen normal $\boldsymbol{n}_s$ and the ϕ axis is about 0.4°. It seems, however, that this error is rather related to the flatness of the thin silicon wafer than to any misalignment: measurements at $x = +3$ mm and $x = -3$ mm differed by only $\Delta(2\theta) = 0.005°$, whereas a difference of $\Delta(2\theta) = 0.015°$ was found when measuring at $x = 0$ and $x = 3$ mm.

If it is assumed that crystal imperfections give rise to less line broadening than the "imperfections" of the experimental set-up, then the rocking curve and the θ–2θ line profile shown in Fig. 6 reflect the horizontal angular divergence and the energy distribution of the X-ray beam. The FWHM of the rocking curve (dashed line) amounts to 0.034°, a value which is of the order of the calculated divergence; using the values listed in Fig. 6, Equation 1 yields 0.026°. One also notices that the intensity of the rocking curve drops to zero once the rock angle no longer permits the crystal to "see" the X-ray source. The interval of 0.076° for which intensity is not zero should be compared with the value of 0.075° characterizing the total divergence $\Delta\theta$ of the beam (see Equation 2).

The θ–2θ line profile (solid curve) clearly resolves the $K\alpha_1$–$K\alpha_2$ doublet ($\Delta\lambda/\lambda = 2.5 \times 10^{-3}$ for the characteristic $K\alpha$ radiation of copper [6]). As expected, the intensity of this curve does not go to zero as for the rocking curve. Each peak $K\alpha_1$ or $K\alpha_2$ has a FWHM of 0.025°, a value which is close to the expected intrinsic line width of Cu$K\alpha$ peaks ($\Delta\lambda \approx 10^{-4}$ nm [6]). It should be noticed that use of a monochromator (in the incident or the diffracted beams) did not reduce appreciably these linewidths but of course suppressed the $K\alpha_2$ peak.

Spatial resolution not reflected by Fig. 6 is determined primarily by the specimen pinhole diameter and by the angle between the incident beam and the specimen surface, both defining the irradiated zone. Choice of the pinhole diameter is dictated by the size of the zone to be investigated and, to some extent, by the desired beam divergence. If small diaphragms are desirable from a point of view of resolution, they increase counting time. With the standard small-focus tube used in our experiment, the reasonable lower limit is 100 μm. Using a rotating anode would reduce this limit to about 30 μm. Finally, the precision for positioning of the zone to be investigated is mainly limited by diffraction of the laser beam at the pinhole. In the present case, the precision is about ± 10 μm. Higher precisions could be attained by the use of a translation stage driven by step-motors and by a more sophisticated interpretation of the distribution of light intensity across the zone.

4. Applications

The angular resolution achieved by triple-axis non-dispersive diffractometers ($\Delta a/a \approx 10^{-7}$ to 10^{-8}) [7, 8] is by far superior to the resolution of the microdiffraction experiment described in this paper ($\Delta a/a \approx 10^{-4}$). However, the purposes of these two experimental set-ups are different. Non-dispersive arrangements are well suited for measuring minute lattice strains or rotations in otherwise homogeneous single crystals. Very small concentrations of carbon in silicon wafers have been measured in this way [7]. High angular resolution is attained with conventional X-ray sources at the expense of localization of the beam (i.e. no collimation).

The microdiffraction experiment makes a compromise between angular and spatial resolutions. It has been specially designed for the analysis of lattice spacing variations or misorientations in heterogeneous materials. The size range of structural inhomogeneities should be in the size range of 50 μm or more if individual features are to be characterized. Lattice imperfections should be larger than the resolution of the experiment (see previous section).

The examples of application presented hereafter have been obtained on directionally solidified dendritic single- and polycrystals. This type of microstructure is frequently encountered in cast alloys [9]. Dendritic single crystals are composed of many dendrites with more or less the same crystallographic orientation. As a result of microsegregation during solidification, these structures display large compositional or even phase heterogeneities with spacings ranging from a few micrometres up to several hundred micrometres. The coarser microstructures are well suited for X-ray microdiffraction measurements within individual dendrites.

4.1. Orientation distribution and three-dimensional arrangement of dendrites

Dendritic single crystals contain many growth defects. In comparison with almost perfect silicon crystals for semiconductor industries, they are of poor quality. In addition to segregations and second-phase precipitates, dendrites are misoriented with respect to each other and their spatial arrangement may vary considerably. Investigation of the relationship between dendrite morphology and crystallography has received much attention over the past decade [9, 10]. Spatial dendrite arrangements have been recently correlated with crystallographic orientation [10].

Berg–Barrett topographs allow one to localize defects and furnish semi-quantitative information

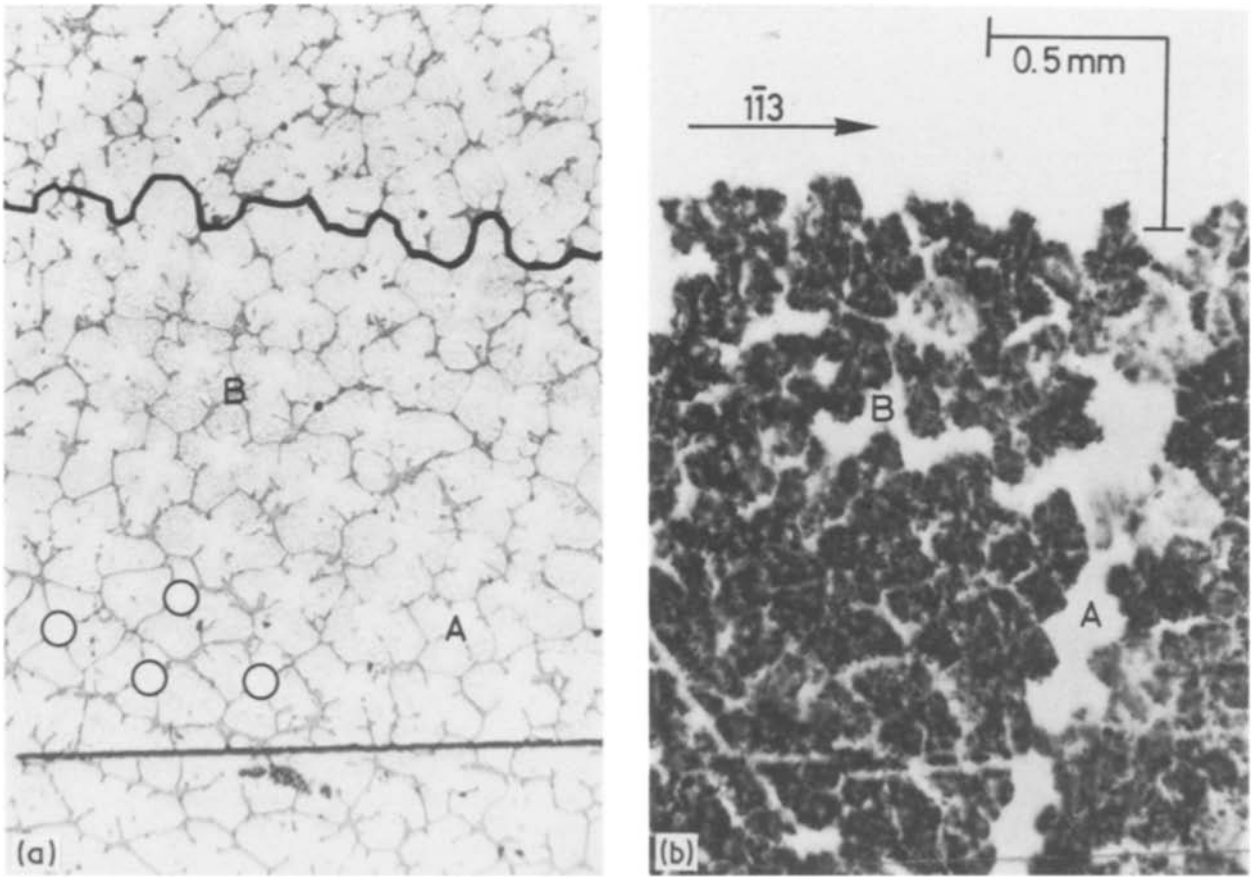

Figure 7 Directionally solidified Ni–Cr–C alloy of hypoeutectic composition. The specimen is cut perpendicularly to the growth direction. In (a) the white phase represents dendrites consisting of a c f c (Ni, Cr, C) solid solution. Dendrite boundaries are outlined by interdendritic eutectic (black lines). Every dendrite looks like a quatrefoiled clover in this transverse section. The dendrite trunks, a few of them being outlined by circles, are at the centre of the clovers. The straight line at the bottom is a reference scratch, whereas the wavy line at the top has been drawn to mark the grain boundary of the bicrystal. (b) A topograph of the same region using the (1 $\bar{1}$ 3) reflection of the c f c (Ni, Cr, C) solid solution and Cu$K\alpha$ radiation. The top grain as well as the interdendritic eutectic do not diffract and therefore appear as white areas and lines, respectively.

about dendrite misorientations. Therefore, they are frequently recorded prior to any microdiffraction experiment: they usually indicate in a straightforward manner zones of interest where quantitative measurements should be performed. Furthermore, they facilitate the interpretation of microdiffraction results. Figs. 7a and b show a micrograph of a directionally solidified Ni–Cr–C alloy and the corresponding topograph, respectively.

The upper part of Fig. 7a represents a second grain of completely different orientation and therefore does not diffract on Fig. 7b (white area). The topograph, which clearly reveals the corrugated shape of the grain boundary, has been used in order to trace this boundary on the micrograph (hand-drawn solid line). In alloys with high amounts of interdendritic eutectic where metallographic etching as a means for revealing grain boundaries frequently fails, this technique has proved to be particularly useful.

Within the diffracting grain, point-to-point correlations between micrograph and topograph can be easily made using reference lines scratched on the specimen surface (straight line at bottom of Fig. 7a). Microstructural features such as interdendritic eutectic regions (dark lines on micrograph) already provide a natural reference system owing to reduced intensity (white lines in Fig. 7b). However, these white lines separating diffracting dendrites (dark areas) can be broader or narrower than on the corresponding micrograph, owing to the so-called "displacement" and "orientation" contrasts [11, 12]. Zone B is a typical example of subgrain boundaries exhibiting a displacement contrast: the adjacent dendrites have a slightly divergent orientation and, accordingly, their diffracting images separate on the topograph. Knowing the distance between the specimen surface and film, the amount of misorientation can be roughly measured. The case of convergent orientations causing the diffracted beams to overlap can also be seen on Fig. 7b.

For displacement contrast to occur, the tilt axis must be approximately in the plane containing the incident and diffracted beams (horizontal arrow line indicated by 1 $\bar{1}$ 3 in Fig. 7b). X-ray topography is much more sensitive to misorientations with vertical tilt axis, giving rise to orientation contrast [11]. The white zone labelled A in Fig. 7b illustrates this kind of misorientation. It can be seen from a comparison with Fig. 7a that, at this place, an entire row of dendrites is missing: a misorientation of more than the FWHM of the rocking curve (see Fig. 10 below) brings this row out of diffraction.

Semi-quantitative observations such as those of Fig. 7 can be complemented by recording topographs with different diffracting planes. Still more detailed

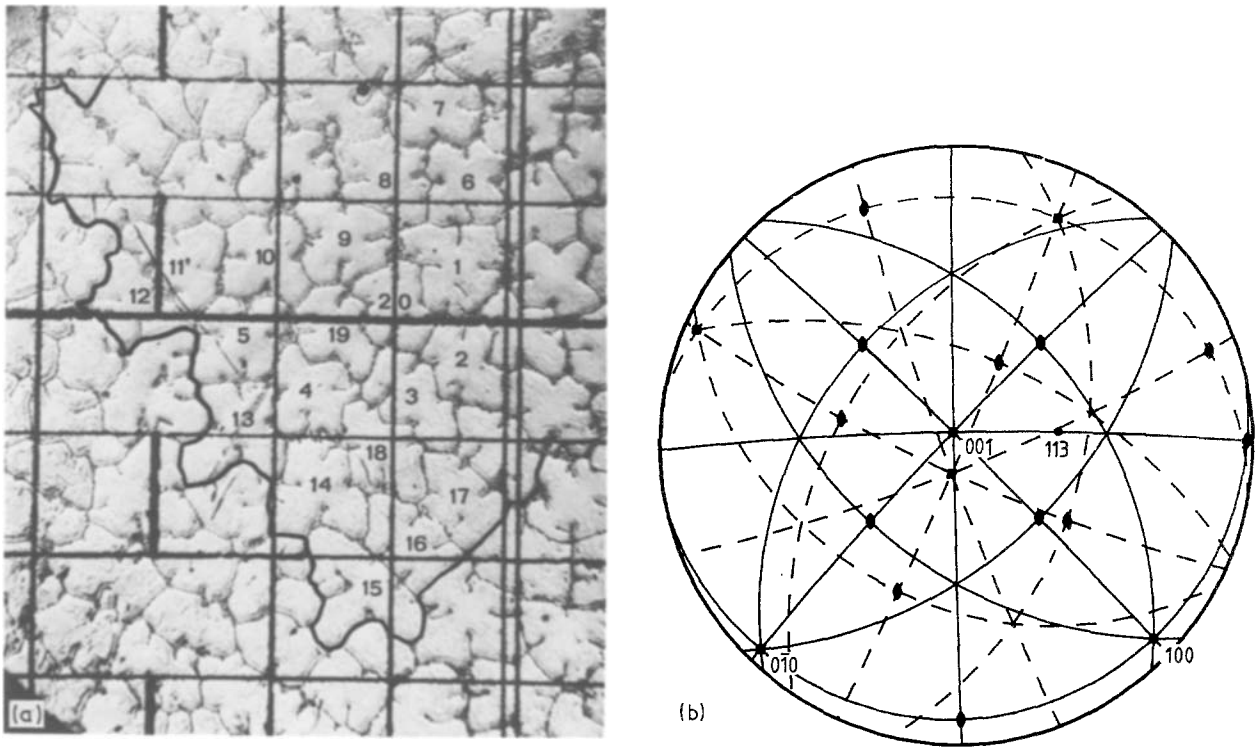

Figure 8 (a) Transverse section of a (Ni, Cr, C) dendritic bicrystal. The square grid is a reference net scratched on the surface. Mesh size: 500 μm. (b) Orientation of the specimen shown in (a). Solid lines: main grain with labelled dendrites; dashed lines: second grain at left. The reference axes of (a) and (b) are the same, i.e. the centre of the stereographic projection corresponds to the specimen surface normal $\boldsymbol{n}_s$.

information is obtained if the orientations of individual dendrites are measured using the microbeam diffraction technique. Fig. 8a shows a transverse micrograph of a bicrystalline dendritic specimen similar to that of Fig. 7a. A grain boundary unambiguously revealed by X-ray topography is again visualized by a hand-drawn solid line.) As far as the orientation of both grains is concerned, the angle between their [0 0 1] directions is about 10° (Fig. 8b). In addition, the two grains are rotated by 20° with respect to each other about the centre of the projection. The dendrite size in Fig. 8a is coarser than in Fig. 7: mean dendrite spacing and trunk diameter are 350 and 180 μm, respectively. A microbeam of 150 μm diameter can therefore easily be positioned in the centre of dendrites without touching neighbouring ones.

Numbered dendrites of Fig. 8a belonging to the central grain were individually placed under the microbeam using the translation stage of the goniometer head. The ϕ, ψ and 2θ angles characterizing the maximum of the $K\alpha_1$ peak were carefully measured for each dendrite trunk. This was done for the (0 0 4) and (1 1 3) reflections indicated in Fig. 8b. The measured values are listed in Table I. From the angles reported in Table I, one can deduce the ($\alpha = \theta - \psi$, ϕ) spherical coordinates of the [0 0 1] and [1 1 3] directions, measured in the reference frame attached to the specimen surface (see Fig. 8). The last column of Table I lists the angles which are found for each dendrite between the two directions. The average angle of 25.33 $\pm$ 0.03° agrees well with the theoretical value of 25.24° if one takes into account that the specimen had to be realigned between the measurements of the two reflections (i.e. precision of the alignment $\pm$0.1°). The [0 0 1] and [1 1 3] directions of each dendrite are plotted in Figs 9a and b. In these extended stereographic projections, the centre ($\alpha = 0°$) corresponds still to the specimen surface normal. The average orientation as well as the solid angle characterizing the orientation distribution have been calculated for each reflection according to the formulae

$$\boldsymbol{r}_m = \frac{\sum_{i=1}^{N} \boldsymbol{r}_i}{N}$$

$$\Omega = \pi \langle \boldsymbol{r}^2 \rangle$$

with

$$\langle \boldsymbol{r}^2 \rangle = \frac{\sum_{i=1}^{N} (\boldsymbol{r}_i - \boldsymbol{r}_m)^2}{N - 1}$$

$\boldsymbol{r}_i$ is the unit vector characterizing the orientation of dendrite i, i.e. $\boldsymbol{r}_i = (\sin \alpha_i \cos \phi_i, \sin \alpha_i \sin \phi_i, \cos \alpha_i)$. These values are listed in Table I. One can notice that, though the ϕ distribution is much larger for the [0 0 1] direction than for [1 1 3], the solid angles are about the same ($\Omega_{001} = 1.04 \times 10^{-4}$ steradian, $\Omega_{113} = 7.7 \times 10^{-5}$ steradian).

Correlations between orientation and spatial distribution of dendrites are useful in studying the growth process of dendritic structures [10, 13]. It can be seen from Fig. 9, for instance, that the orientations of dendrite trunks are much more dispersed along a direction linking dendrites 12 and 14 than along another direction linking dendrites 3 and 14. These observations can be related to the mechanisms of dendritic branching and to the constraints occurring during growth.

TABLE I 2θ, ψ and ϕ angles measured for the numbered dendrites of Fig. 8a, using the (0 0 4) and (1 1 3) reflections. Cu$K\alpha$ radiation. (The spherical coordinates of these orientations are simply given by: $\alpha = \theta - \psi$ and ϕ.) The angles between [0 0 1] and [1 1 3] as deduced from these measurements are listed in the last column. Average values of 2θ and of a are listed at the bottom together with the mean orientations and solid angles Ω characterizing the orientation distribution of these points

Dendrite No.	(0 0 4) reflection			(1 1 3) reflection			Angle between [0 0 1] and [1 1 3] (theory = 25.24°)
	2θ	ψ	ϕ	2θ	ψ	ϕ	
1	120.50	56.93	0.0	92.06	68.57	35.04	25.33
2	120.50	56.80	−2.2	92.07	68.61	35.55	25.39
3	120.50	56.57	−2.5	92.07	68.41	35.98	25.35
4	120.51	56.77	−1.2	92.07	68.51	35.66	25.35
5	120.50	56.91	−2.4	92.06	68.72	35.00	25.36
6	120.48	56.92	1.7	92.06	68.51	34.82	25.32
7	120.49	56.94	3.0	92.06	68.50	34.80	25.34
8	120.46	56.85	4.8	92.05	68.33	34.72	25.29
9	120.48	56.84	5.5	92.05	68.32	34.54	25.32
10	120.47	56.96	−6.0	92.04	68.39	34.20	25.30
11	120.48	57.07	2.5	92.05	68.56	34.66	25.27
12	120.43	57.11	4.3	92.05	68.62	34.34	25.33
13	120.46	56.91	−1.6	92.05	68.60	35.08	25.31
14	120.50	56.64	−4.6	92.06	68.52	35.64	25.35
15	120.52	56.26	−7.8	92.07	68.39	36.72	25.36
Average $\langle 2\theta \rangle$	120.485 ± 0.023°			92.058 ± 0.009°			
Average $\langle a \rangle$	0.35491 ± 0.00004 nm			0.35498 ± 0.00003 nm			
Average orientation $\langle \alpha \rangle$	3.4°			22.47°			
$\langle \phi \rangle$	0.2°			35.12°			
Solid angle, Ω (sr)	1.04×10^{-4}			7.7×10^{-5}			

4.2. Lattice spacing

As observed on Table I, the 2θ values measured for the various dendrite trunks do not differ significantly. From the average and the standard deviation, one calculates the lattice parameters $a = 0.35491 \pm 0.00004$ nm and $a = 0.35498 \pm 0.00003$ nm from the (0 0 4) and (1 1 3) reflections, respectively. Considering the values reported by Taylor and Floyd [14] for Ni–Cr alloys, one finds a chromium concentration of about 18.5 at % in solid solution within the dendrite trunks. This agrees quite well with the value one can expect by subtracting from the starting composition the chromium atoms which are contained in the Cr_7C_3 interdendritic precipitates.

4.3. Mosaïc structure and lattice spacing distribution

The dendrite orientations reported in Fig. 9 correspond to the maximum of the $K\alpha_1$ peak with the X-ray beam of 0.15 mm diameter being positioned precisely on the corresponding trunk. The microdiffraction experiment permits us to measure the orientation distribution (i.e. the mosaïc structure) as well as the distribution of lattice spacings within the irradiated zone. The two curves plotted in Fig. 10 represent a rocking curve and a θ–2θ line profile for a single dendrite trunk ([0 0 2] reflection of the (Ni, Cr, C) solid solution, Cu$K\alpha$ radiation). These curves can be directly compared with those measured for the silicon single

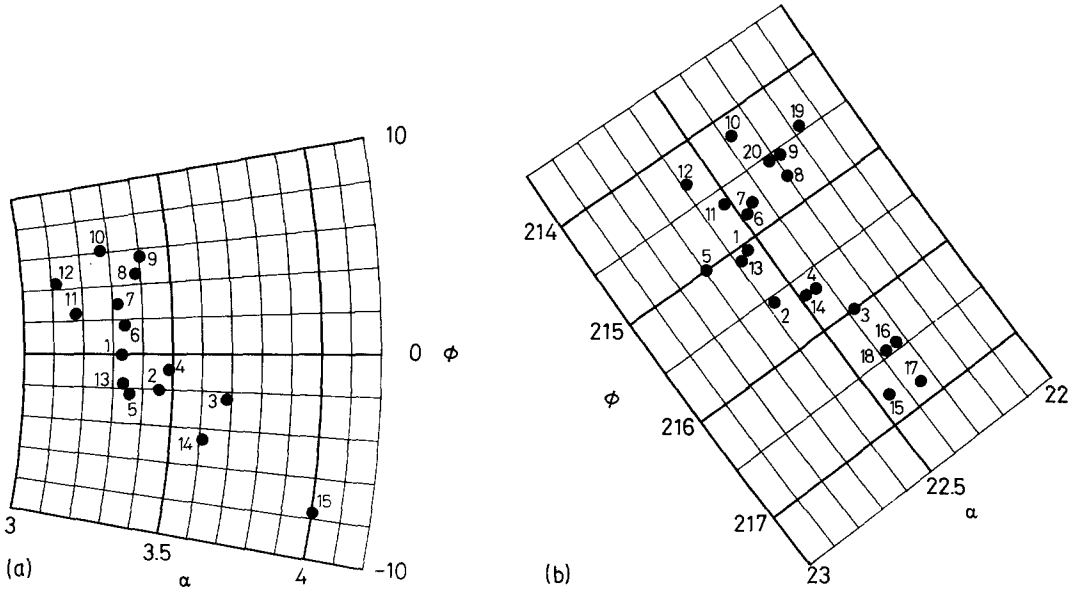

Figure 9 Extended stereographic projections of the orientation shown in Fig. 8b. The enlargements correspond to zones surrounding (a) [0 0 1], and (b) [1 1 3] directions. (A rotation around the centre of the stereographic projection has been performed between Figs 8b and 9.) Points on the projections correspond to the orientations of labelled dendritic trunks in Fig. 8a, as measured by microbeam diffraction (see Table I).

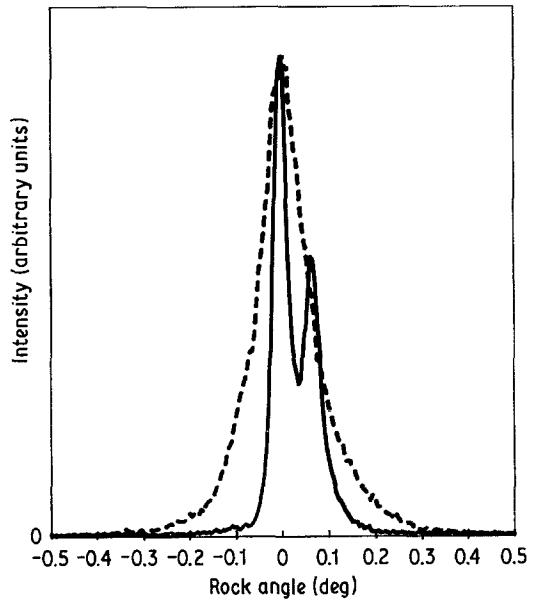

Figure 10 Rocking curve (dashed line) and θ–2θ line profile (solid line) of the (0 0 2) reflection of a (0 0 1) dendritic specimen. Cu$K\alpha$ radiation. The measurement was made on an individual dendrite trunk of the specimen shown in Fig. 8a. $\psi = 25.745° \pm 0.5°$. Φ_x = 0.1 mm, Φ_s = 0.15 mm, detector cross-slit 0.15 mm × 2 mm, d_{xs} = 190 mm, d_s = 20 mm, D = 200 mm. Counting time: 30 sec for each step.

crystal (Fig. 6) since the diffraction conditions were about the same (i.e. same diaphragms, symmetrical reflection in both cases, Bragg angles differing by about 9°).

First, the rocking curve for dendrites is much larger than the rocking curve reflecting the "imperfections" of the experimental set-up: the FWHM is 0.12° in Fig. 10 and the tails of the peak extend to over 0.6°. Assuming Lorentzian line shapes and an apparent intrinsic line width of FWHM = 0.034° (Fig. 6), the difference of line widths representing the FWHM of the mosaïc structure is found to be 0.09° (i.e. a value 3 times larger than the corresponding one measured from Fig. 6). The large extension of the peak tails, indicating that some parts of the dendrite trunk may be largely misoriented, was confirmed by recording several topographs at various angles. Figs 9 and 10 together provide a rather good general view of the dendrite orientations: each point in the extended stereographic projections of Fig. 9 represents a separate peak whose solid angle at half the maximum intensity is about 3×10^{-6} steradian.

Second, the $K\alpha_1$ and $K\alpha_2$ peaks of the θ–2θ curve in Fig. 10 are slightly broadened (0.034° as compared to 0.025° in Fig. 6) as can be seen from the increased overlap of these two peaks. Since broadening is small, exact calculation of the intrinsic lattice spacing distribution would require peak deconvolution and measurement of an (Ni, Cr) "perfect" single crystal under the same diffraction conditions (i.e. identical Bragg angle). Without this information, an approximate value for the distribution of lattice spacings is obtained by again assuming Lorentzian line shapes. The broadening of 0.009° found in this way for the $K\alpha_1$ or $K\alpha_2$ peaks would correspond to $\Delta a/a \approx 3.2 \times 10^{-4}$. If interpreted as a variation of chromium concentration c within the dendrite trunk, this small value corresponds to $\Delta c \approx 0.9$ at % [14].

5. Conclusions

The operational modes of this new device are very similar to the dark-field mode in TEM. This latter technique has a much higher spatial resolution, whereas our X-ray set-up provides a superior angular resolution and permits one to investigate long-distance effects due to an almost unlimited size of the specimen. The foregoing examples of application have been chosen to illustrate the benefits of combining X-ray topography and microbeam diffraction in a single device.

Berg–Barrett topography can take advantage of the rotational facility provided by the four-circle goniometer. In particular, it is possible to record topographs at well chosen positions of the rocking curve and thus to visualize the various diffracting parts of the specimen. Similarly, topographs can be taken while oscillating the specimen during exposure within a given angular interval. The orientation distribution of dendrites in a single-crystalline turbine blade has been determined in this way [15]. On the other hand, X-ray microbeam diffraction takes full advantage of spatial information furnished by topography. This mode of operation has been used for the investigation of plastic deformation in the sub-surface layer of specimens tested in abrasive wear [16] and for the identification of slip systems and localization of plastic deformation in Ni–Cr–C and Ni–Al–Cr–C alloys [17, 18].

X-ray topography has been traditionally applied to study isolated defects in otherwise almost perfect single crystals such as dislocations in silicon crystals [19, 20]. The extinction contrast revealing these isolated defects is normally screened by misorientation contrasts when more complex defect structures are present, after heavy plastic deformation or at the tip of propagating crack [21–25]. All applications, ours included, have in common that typical features to be investigated must be surrounded by reference areas sufficiently free of defects to allow any particular contrast to appear. This again is a problem of size, restricting the type of materials to be analysed in this way. One further condition for topographical observations of heterogeneous structures is to chose the appropriate beam divergence: if it is too high, resolution is poor and if too low, the few microstructural features selected for diffraction do not permit one to establish long-distance correlations. Selection of the beam divergence depends on the orientation distribution of the whole specimen and on the rocking curve line width of individual microstructural features.

The restrictions in X-ray microbeam diffraction are also related to the specimen characteristics. The size of the beam should obviously be smaller than the smallest feature to be characterized, whereas angular divergence and energy dispersion should be inferior to the corresponding intrinsic line widths of the specimen. At present, spatial resolution in microbeam diffraction is limited to selected areas of about 100 μm diameter. Limitations are due to long exposure times

as a result of the relatively low flux density of the X-ray beam. Use of a high intensity source (rotating anode or synchrotron radiation), possibly combined with a position-sensitive detector, would allow one to decrease this limit to about 10 μm. Spatial resolution in microbeam diffraction and topography would then be almost identical. The field of application of this technique could thereby be extended to heterogeneous materials with still finer structures.

The characteristics of the experimental set-up presented in this paper have been optimized for the analysis of dendritic microstructures. However, any material exhibiting heterogeneities in the same size range could be analysed in this way. In order to take full advantage of the present device, these inhomogeneities (which may be associated with microstructure or with plastic deformation) should give rise to misorientations of at least a few hundredths of a degree and/or to lattice spacing variations greater than 10^{-4}.

Appendix

If the irradiated zone of the specimen surface is not precisely located at the centre O of the four-circle goniometer (see Fig. 11), inaccurate 2θ values will result. Supposing that the surface is displaced by an amount Δz (dashed surface) with respect to the exact position (solid line), the "dashed" diffracted beam s_d remains at the same 2θ value but the detector has to be turned by $\Delta(2\theta)$ around Point O in order to receive the signal. Approximately:

$$\tan [\Delta(2\theta)] \approx \Delta(2\theta) = \frac{\Delta z'}{D} \qquad \text{(A1)}$$

where $\Delta z'$ is the distance separating the diffracted beams when the surface is translated by Δz, and D is the surface-to-detector distance. If θ is the Bragg angle and α the angle between specimen surface and diffracting planes $(h\,k\,l)$, the following relationship is obtained:

$$\Delta z_p = \frac{\Delta z}{\sin(\theta + \alpha)} = \frac{\Delta z'}{\sin(2\theta)} \qquad \text{(A2)}$$

Therefore, using Equations A1 and A2 and differentiating Bragg's law, one gets

$$\left|\frac{\Delta a}{a}\right| = \left|\frac{\Delta\theta}{\tan\theta}\right| = \frac{\Delta z}{D}\frac{\cos^2\theta}{\sin(\theta + \alpha)} \qquad \text{(A3)}$$

This error decreases as θ increases. The term $\sin(\theta + \alpha)$ in the denominator shows clearly that the position chosen in Fig. 11 is for diffractometric studies as compared to the reverse situation where $(\theta - \alpha)$ would be the angle between the incident beam and the surface.

Now suppose that a translation is made along an axis which is not exactly in the surface plane (mismatching of the normal n_s and the ϕ axis in Fig. 5). In this case, a translation x of the surface will give an "apparent" $\Delta a/a$ variation:

$$\frac{\Delta a}{a} = \frac{\delta x}{D}\frac{\cos^2\theta}{\sin(\theta + \alpha)} \qquad \text{(A4)}$$

where δ is the misalignment angle between the surface and the translation axis, measured in radians.

The incident angle $(\theta + \alpha)$ not only reduces the error $\Delta a/a$ owing to inaccurate specimen positioning, it also reduces the size of the X-ray spot on the specimen surface. Projection of the specimen diaphragm Φ_s on the specimen surface gives

$$(\Phi_s)_p = \frac{\Phi_s}{\sin(\theta + \alpha)} \qquad \text{(A5)}$$

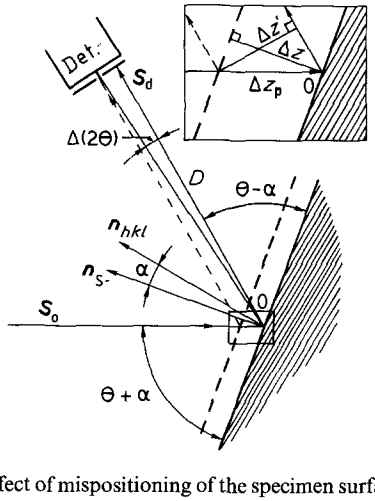

Figure 11 Effect of mispositioning of the specimen surface on microdiffraction measurements.

Acknowledgement

This research was supported by the Swiss National Fund for Scientific Research.

References

1. B. K. TANNER and D. K. BOWEN (eds), "Characterization of Crystal Growth Defects by X-ray Methods", Nato Advanced Study Institute Series, Vol. 63 (Plenum Press, New York, 1980).
2. B. K. TANNER, "X-ray Diffraction Topography" (Pergamon Press, Oxford, 1976).
3. SHUJI TAIRA (ed), "X-ray Studies on Mechanical Behavior of Materials" (The Society of Materials Science, Kyoto, 1974).
4. J. B. NEWKIRK, *Trans. Met. Soc. AIME* **215** (1959) 483.
5. T. KONAGA, in "X-ray Studies on Mechanical Behaviour of Materials", ed. S. Taira (The Society of Materials Science, Kyoto, 1974) p. 205.
6. B. D. CULLITY, "Elements of X-ray Diffraction", 2nd Edn (Addison-Wesley, Reading, Massachusetts, 1978).
7. M. A. PICK, K. BICKMANN, E. POFAHL, K. ZWOHL and H. WENZL, *J. Appl. Cryst.* **10** (1977) 450.
8. B. C. LARSON and W. SCHMATZ, *Phys. Rev.* **B10** (1974) 2307.
9. W. KURZ and D. J. FISHER, "Fundamentals of Solidification" (Trans Tech, Aedermannsdorf, Switzerland, 1984).
10. M. RAPPAZ and E. BLANK, *J. Cryst. Growth* **74** (1986) 67.
11. M. WILKENS, *Can. J. Phys.* **45** (1967) 567.
12. R. W. ARMSTRONG, W. J. BOETTINGER and M. KURIYAMA, *J. Appl. Cryst.* **13** (1980) 417.
13. E. BLANK and M. KASPAR, in preparation.
14. A. TAYLOR and R. W. FLOYD, *J. Inst. Met.* **80** (1952) 577.
15. M. RAPPAZ, M. KASPAR and E. BLANK, in Proceedings of 5th Risø International Symposium on Metallurgy and Materials Science, edited by N. H. Andersen, M. Eldrup, N. Hansen, D. J. Jensen, T. Leffers, H. Lilholt, O. B. Pedersen and B. W. Singh (Risø National Laboratory, Roskilde, Denmark, 1984) p. 443.

16. M. RAPPAZ and E. BLANK, *Wear* **84** (1983) 387.
17. M. RAPPAZ and E. BLANK, in Proceedings of 3rd International Symposium on Metallurgy and Materials Science, edited by H. Lilholt and R. Talreja (Risø National Laboratory, Roskilde, Denmark, 1982) p. 285.
18. E. BLANK, M. KASPAR and M. RAPPAZ, in Proceedings of 7th International Conference on Strength of Metals and Alloys (ICSMA-7), edited by H. J. MacQueen, P. Bailen, J. I. Dickson, J. J. Jones and M. G. Akben (Pergamon Press, Montreal, 1985) p. 87.
19. A. R. LANG, in "Diffraction and Imaging Technique in Materials Science", Vol. II edited by S. Amelinckx, R. Gevers and J. Van Landuyt (North-Holland, Amsterdam, 1978) p. 623.
20. A. AUTHIER, *ibid.* p. 715.
21. T. LARCHUK, T. KATO, R. N. PANGBORN and J. C. CONWAY Jr, in "Applications of X-ray Topographic Methods to Materials Science", edited by S. Weissmann, F. Balibar and J.-F. Petroff (Plenum Press, New York, 1984) p. 301.
22. W. E. MAYO and S. WEISSMANN, *ibid.* p. 311.
23. G. MICHOT, A. GEORGE and G. CHAMPIER, *ibid.* p. 325.
24. J. C. BILELLO, *ibid.* p. 333.
25. A. B. HMELO, J. C. BILELLO, S. T. DAVIES and D. K. BOWEN, *ibid.* p. 343.

Received 18 April
and accepted 30 June 1986